3rd International Symposium on Integrating CFD and Experiments in Aerodynamics
20-21 June 2007
U.S. Air Force Academy, CO, USA

Static Extended Trailing Edge for Lift Enhancement: Experimental and Computational Studies

T. Liu,* Montefort, W.W. Liou, and S. R. Pantula
Department of Mechanical and Aeronautical Engineering
Western Michigan University, Kalamazoo, MI 29008
*tianshu.liu@wmich.edu

Q. A. Shams
NASA Langley Research Center, Hampton, VA 23681
q.a.shams@larc.nasa.gov

Abstract

A static extended trailing edge attached to a NACA0012 airfoil section is studied for achieving lift enhancement at a small drag penalty. It is indicated that the thin extended trailing edge can enhance the lift while the zero-lift drag is not significantly increased. Experiments and calculations are conducted to compare the aerodynamic characteristics of the extended trailing edge with those of Gurney flap and conventional flap. The extended trailing edge, as a simple mechanical device added on a wing without altering the basic configuration, has a good potential to improve the cruise flight efficiency.

Key words: trailing edge, airfoil, wing, lift, drag, aerodynamics

Introduction

It has long been recognized that flaps can significantly alter wing aerodynamics for high lift generation. Conventional flaps have larger drag; therefore they are mainly deployed for takeoff and landing and are not suitable in cruise flight. Small trailing edge devices like Gurney flaps and divergent trailing edges for lift enhancement have attracted considerable attention in aeronautical community. The Gurney flap was introduced by Liebeck [1] for aeronautical applications, and considerable measurements and calculations have been performed to determine the aerodynamic characteristics of wings with Gurney flaps at low speeds [2-9]. Measurements were also made at high speeds [10]. Gurney-flap-type tabs have been used along with vortex generators to enhance lift and suppress flow separation for a single-slotted-flap airfoil at large flap deflection [11]. Microflaps that can change the deflection angle were used for flutter suppression [12]. To mimic the behavior of bird feathers during landing, a self-adjusting movable flap close to the trailing edge was proposed by Bechert et al. [13], which was able to maintain higher lift when stall occurs. A review on trailing edge devices and other control technologies is given by Stanewsky [14].

Measurements of avian wing geometry for extracting typical avian airfoil sections indicate that the merganser and owl wings have a very thin trailing edge that is a single layer of feathers extended from a 'normal' airfoil section [15]. Naturally, a question is whether and how this unique trailing edge affects the global aerodynamic characteristics of the wing. This inspires the concept of a static extended trailing edge (SETE) as illustrated in Figure 1(a). The main airfoil element remains unchanged, but it is extended at the trailing edge by attaching a thin splitting plate of suitable length and rigidity. As shown in Fig. 1(b), the basic geometrical parameters are the main airfoil chord (c), length of SETE (l) and deflection angle (δ). Depending on specific applications, the extension could be an aluminum plate, polymer membrane, composite sheet or smart material plate. In general, a thin extended trailing edge is flexible such that it can be passively changed through flow-structure interaction or actively controlled by embedded actuators. In the current operating conditions, our analysis shows that when extended trailing edges are sufficiently rigid, their shapes are not sufficiently affected by flow and no vibration is induced. Thus, the cases studied here are static or quasi-steady. The effects of SETE on the wing aerodynamics are mainly due to modifications of the airfoil camber and of the flow structure at the trailing edge. The lift enhancement by SETE is expectedly due to the camber effect. It is speculated that the drag penalty of SETE is small since it is

usually embedded in the wake of the main airfoil. The drag penalty should be examined carefully in comparison with Gurney flaps and conventional flaps. The objective of this work is to study SETE as an alternative flow control technique for lift enhancement at a small drag penalty in cruise flight.

We first describe the geometrical features of SETE and relevant similarity parameters. Experimental results are presented including the lift and drag coefficients of the baseline NACA0012 airfoil model and model with SETE and Gurney flaps. The lift enhancement is achieved by SETE, while the drag polar and lift-to-drag ratio remains largely unchanged. The zero-lift drag and Oswald efficiency are not significantly affected by SETE. The benefit analysis for SETE in cruise flight is given in comparison with Gurney flap. Based on thin airfoil theory and CFD simulations, the aerodynamic characteristics of SETE are further compared with those of the corresponding Gurney flap and conventional flap.

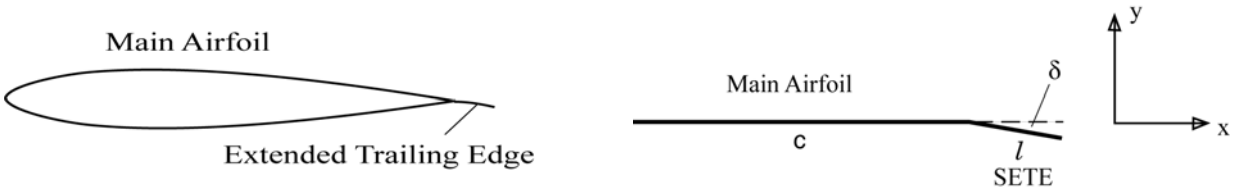

(a) (b)

Figure 1. (a) Illustration of an extended trailing edge, (b) Geometrical parameters and coordinate system.

The team members of experimentalists and computationalists are fully engaged throughout the various phases of the research. The open and continuous communications have facilitated the planning, the design, and the execution of experimental and computational tasks. In fact, they often lead to valuable insights that are not readily apparent to a uni-approach team. We believe a full integration of experimental and numerical approaches can be very effective and cost-efficient for aerodynamics studies.

Wind Tunnel and Model

Tests were conducted in the Advanced Design Wind Tunnel (ADWT) at Western Michigan University (WMU). The ADWT is a low speed, closed circuit single return, atmospheric tunnel with a test section of 32 inches high, 45 inches wide, and 8 feet long. Full test section length Plexiglas windows on sides and ceiling allow optical access. The 161 feet long circuit consists of two legs of 65.6 feet long and the other two legs of 14.9 feet long. Low turbulence and good flow direction control are obtained by a combination of features, including four screens and honeycomb in the stilling camber, a 10:1 contraction ratio between the stilling chamber and test section, empirically tailored test section walls, tangential flow breathing at the test section exit to the diffuser, and a 5.4^o diffuser angle. Under the present test conditions at $Re_c = 4.74 \times 10^5$, natural boundary layer transition was observed at about 30%c on the NACA0012 airfoil model at zero AoA based on global luminescent oil film skin friction measurements [16]. The main drive power source is a 125 hp DC motor with a solid-state speed controller. The 16-blade fan is 6 feet in diameter. The flow velocity range is approximately 20 to 240 ft/sec (6 to 73 m/sec) where the total temperature is in the range of 60 to 120^o F. This corresponds to the dynamic pressures up to 65 lb/ft^2 and Reynolds numbers up to 1.3 $\times$ 10^6 per foot.

A six–component internal force balance (AeroLab) is installed in the ADWT. The balance measurement ranges are ±150 lb for lift, ±100 lb for side force, ±25 lb for axial force, ±250 in-lb for pitching moment, ±180 in-lb for yawing moment, and ±200 in-lb for rolling moment. A parallelogram linkage sting support system is able to set the angle of attack from –36^o to 36^o within the accuracy of 0.1^o. A traverse system of two degrees of freedom is equipped for probes.

A ceramic NACA0012 airfoil section model was used in experiments. The chord and span of the model were 10 in and 12 in, respectively. Along the wing span, two 1.875-in long and 6-in wide parts made of polycarbonate can be

mounted to the baseline model with 4 screws for clamping SETE at the trailing edge, and they can be easily removed to place different extended trailing edges. Several pieces of SETE with different lengths were prepared for tests, which were made of either aluminum or Mylar (PET-polyester). The Young's modulus and Poisson ratio for aluminum were 70 GPa and 0.35, respectively, while the Young's modulus and Poisson ratio for Mylar were 2.8 GPa and 0.37, respectively. Figure 2 shows the NACA0012 airfoil model attached with a Mylar SETE, and the model parts before assembly, including the baseline NACA0012 model, two removable parts for clamping SETE, and typical aluminum SETE and Mylar SETE. In order to support the model, the end plates (18 by 13 in) were mounted to the sting balance through two aluminum bars placed in a mounting bracket. The end plates also reduced the three-dimensionality of flow. Figure 3 shows the model mounted on the balance for testing in the ADWT.

(a) (b)

Figure 2. (a) NACA0012 airfoil model with a Mylar SETE, (b) Baseline model, removable parts, and aluminum SETE and Mylar SETE.

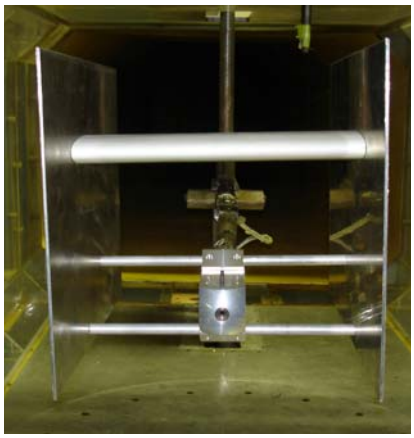

Figure 3. NACA0012 airfoil model mounted on the end plates connected to in a sting balance.

Similarity Parameters

The similarity parameters for a rigid airfoil with an extended trailing edge are considered. The similarity parameters for a rigid airfoil are Reynolds number $Re_c = U_\infty c / \nu$ and Mach number M_∞, where U_∞ is the freestream velocity and c is the airfoil chord. Since an extended trailing edge is attached to the rigid airfoil, additional similarity parameters should be obtained for achieving the complete flow and structure similarity. An extended trailing edge is generally considered to be flexible as a thin cantilever plate deforming under aerodynamic loading. The differential

equation for the time-independent displacement *w* of a thin plate is generally expressed by $L[w(x,y)] = F(x,y)$ [17], where *x* and *y* are the chordwise and normal coordinates, respectively, *L* is a linear differential operator, and $F(x,y)$ is an external distributed force on the plate. In our case, $F(x,y) = \Delta p$ is the aerodynamic pressure difference across the plate or aerodynamic load. For a homogenous plate, the operator $L = D_E \nabla^4$ is the bi-harmonic operator, where $D_E = Eh^3 / 12(1-\nu^2)$ is the plate flexural rigidity. The rigidity D_E depends on the plate thickness (*h*), Young's modulus (*E*), and Poisson ratio (ν).

Let us introduce the following the non-dimensional variables $\overline{F} = F / q_\infty$, $\overline{w} = w / l$, $\overline{x} = x / l$, $\overline{y} = y / l$, where $q_\infty = \rho_\infty U_\infty^2 / 2$ is the dynamical pressure and *l* is the length of SETE. Thus, we have the non-dimensional equation $G_1 \nabla^4 \overline{w} = \overline{F}$, where the main similarity parameter for aeroelasticity is $G_1 = D_E / (l^3 q_\infty)$. The functional relations for the lift and drag coefficients are $C_L = f_1(\alpha, Re_c, M_\infty, G_1, \delta, l/c)$ and $C_D = f_2(\alpha, Re_c, M_\infty, G_1, \delta, l/c)$. For SETE, the similarity parameter G_1 should be sufficiently large such that the shape of SETE is not changed significantly by flow. For the present low-speed experiments, M_∞ is very small and Re_c is fixed at 4.74×10^5. Although the effects of Re_c and M_∞ are worthwhile for further investigation, we mainly consider here the aerodynamic behavior of the NACA0012 airfoil model with SETE in the parametric space $(\alpha, \delta, l/c)$.

Results and Discussions

Static Extended Trailing Edge

Figure 4 shows the lift and drag coefficients as a function of angle of attack (AoA) for the baseline NACA0012 airfoil model at $Re_c = 4.74 \times 10^5$. According to McCormick's formula [18], the lift slope depends on the aspect ratio (AR) by

$$a = \frac{dC_L}{d\alpha} = \frac{a_0 AR}{AR + 2(AR+4)/(AR+2)}, \tag{1}$$

where $a_0 = 2\pi$ according to thin airfoil theory. As shown in Fig. 4, a fit to the lift data of the baseline model using Eq. (1) gives the effective aspect ratio $AR = 4.42$ that is larger than the physical aspect ratio of 1.2. The end plates substantially reduced the three-dimensionality of flow. As shown in Fig. 5, the drag coefficient is represented as a function of the lift coefficient squared and fitted using the classical relation $C_D = C_{D0} + C_L^2 / \pi e AR$. Therefore, we obtain the zero-lift drag coefficient $C_{D0} = 0.014$ and the Oswald span efficiency $e = 0.8$ for $AR = 4.42$. Although the finite end plates do not completely eliminate the three-dimensionality of flow, they modify the tip vortices acting like large winglets.

In tests, an aluminum sheet (0.216 mm thick) and a Mylar sheet (0.254 mm thick) have been used as SETE, whose deflection angle was set a priori. The plate flexural rigidities of the aluminum sheet and Mylar sheet are $D_E = 0.067\ Nm$ and $D_E = 0.0044\ Nm$, respectively. Figure 6 shows the lift coefficient as a function of AoA and drag polar for the model with SETE at $Re_c = 4.74 \times 10^5$, where C_L and C_D are based on the projected wing area of the baseline model. The lengths of SETE are 5% and 10% of the chord of the baseline model, and the preset deflection angles of SETE are 0, 5, 7 and 10 degrees. According to Fig. 6, the C_L distribution is shifted up and the lift is enhanced depending on the deflection angle and relative length of SETE, while the drag polar basically remains unchanged. The drag polar curves are collapsed for different deflection angles, indicating that the zero-lift drag and Oswald efficiency are not changed. Stall occurs a few degrees earlier particularly for larger deflections. For the model with zero deflection, C_L is almost the same as that of the baseline model when AoA is less than 10^o, but it is larger for higher AoA until stall. Typically, four and five repeated tests were conducted for each case, and

the results were averaged. The measurement uncertainties in C_L are 0.001 for low AoA and 0.01 for high AoA. For C_D, the measurement errors are 0.0002 for low AoA and 0.003 for high AoA.

Further, the drag coefficient is plotted as a function of the lift coefficient squared, as shown in Fig. 7(a). All the data are basically collapsed into a single straight line, which is consistent with Fig. 6(b). Both the zero-lift drag coefficient and Oswald efficiency do not significantly change within the measurement accuracy for different deflection angles (small enough) and lengths of SETE. It is indicated in Fig. 7(a) that the increased C_D results mainly from an increase of the induced drag $C_L^2 / \pi e AR$ associated with the lift enhancement by SETE. It is expected that this drag penalty will be reduced as the aspect ratio increases. To examine the aerodynamic effectiveness of SETE, the lift-to-drag ratio (L/D) is plotted in Fig. 7(b) as a function of C_L. The plots of L/D against C_L are approximately collapsed. One implication is that SETE is able to increase C_L while the variation in L/D is relatively small. The significance of these findings is that SETE could improve the aerodynamic efficiency of cruise flight.

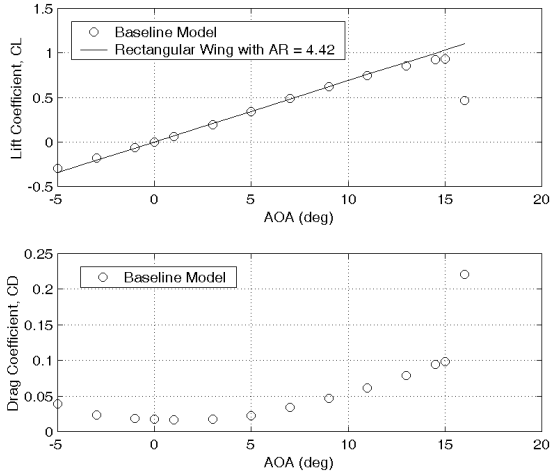

Figure 4. Lift and drag coefficients as a function of AoA for the baseline NACA0012 airfoil model at $Re_c = 4.74 \times 10^5$.

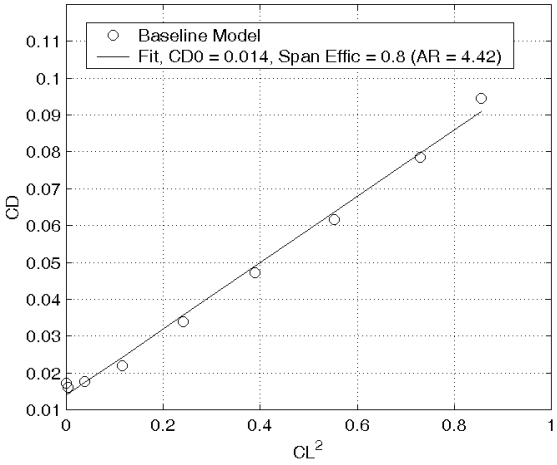

Figure 5. Drag coefficient as a function of the lift coefficient squared for the baseline NACA0012 airfoil model at $Re_c = 4.74 \times 10^5$.

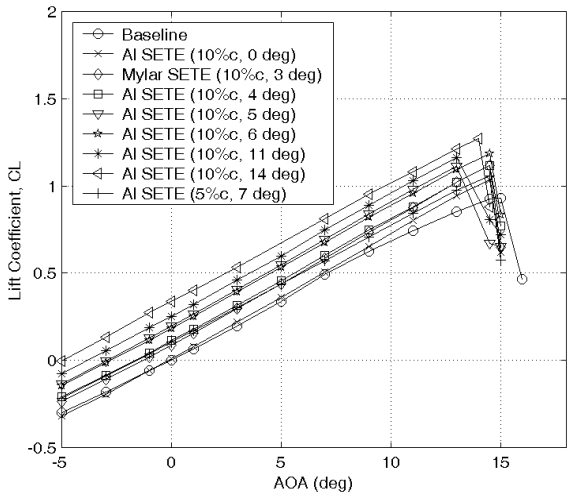

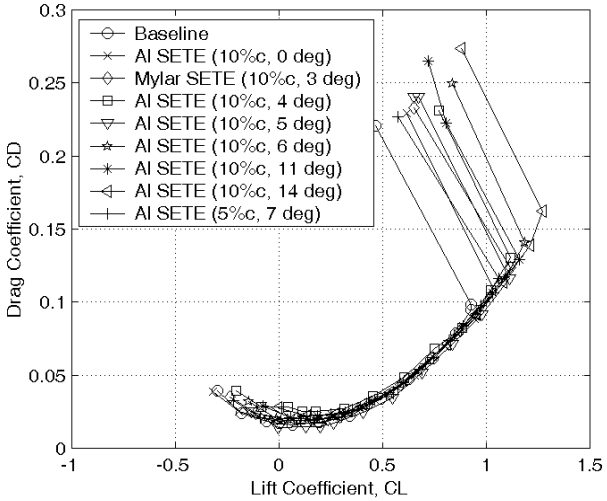

(a) (b)

Figure 6. (a) Lift coefficient as a function of AoA and (b) drag polar for the NACA0012 airfoil model with SETE at $Re_c = 4.74 \times 10^5$.

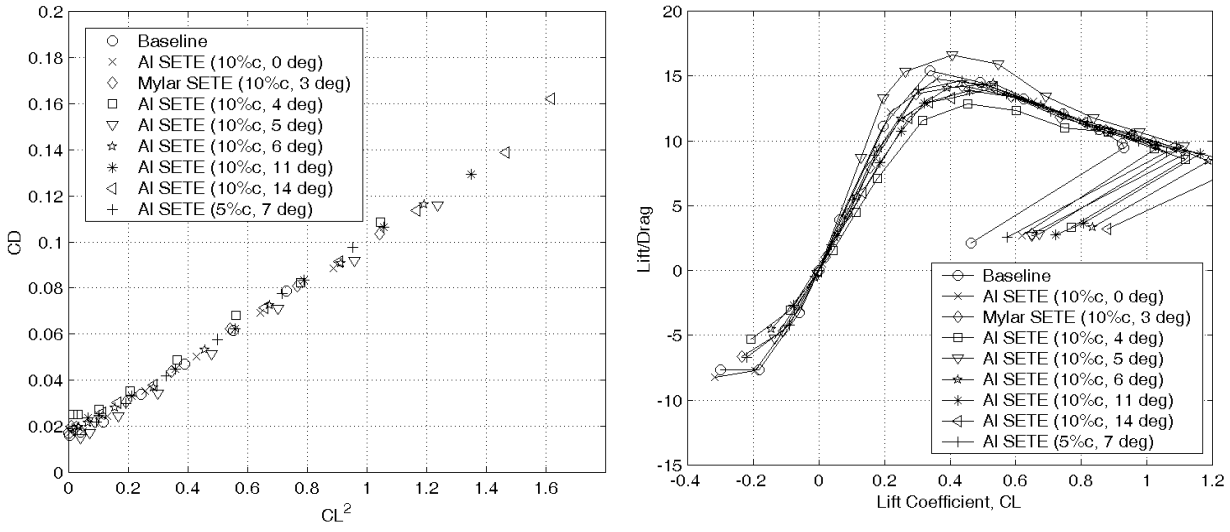

(a) (b)

Figure 7. (a) Drag coefficient as a function of the lift coefficient squared, (b) Lift-to-drag ratio and as a function of the lift coefficient for the NACA0012 airfoil model with SETE at $Re_c = 4.74 \times 10^5$.

Comparison with Gurney Flaps

The aerodynamic characteristics of SETE are compared with those of Gurney flap, which is a short wall attached to the trailing edge that is perpendicular to the chord line on the pressure side of an airfoil, as illustrated in Fig. 8. Both SETE and Gurney flap increase the lift at the cost of increasing the drag. However, there are some important quantitative differences between SETE and Gurney flaps on the drag penalty. The measured results by Li et al. [7] for a NACA0012 rectangular wing indicate that L/D as a function of C_L for the wing with Gurney flaps (0.5-3%c heights) are significantly lower than that for the baseline wing except at higher C_L. Unlike SETE, the curves of L/D as a function of C_L for Gurney flaps do not collapsed. Similar results can be found for other wings with Gurney flaps. The general conclusion is that Gurney flaps are not suitable for cruise flight due to the reduced L/D by the larger drag penalty. After fitting the data of Li et al. [7] using $C_D = C_{D0} + C_L^2 / \pi e AR$, it is found that the zero-lift drag coefficient C_{D0} increases in a roughly linear fashion from 0.0065 for the baseline model to 0.021 for the 3%c high Gurney flap, where the effective aspect ratio is 46.5. The drag increase is caused by the extra form drag associated with open flow separation behind a Gurney flap.

To provide a direct comparison of SETE with Gurney flaps, Gurney flap measurements were conducted using the same baseline NACA0012 airfoil model with the same chord Reynolds number. The Gurney flap height ranges from 1.2%c to 6.75%c. Figure 8(b) shows the NACA0012 airfoil model with a Gurney flap. Figure 9 shows the lift coefficient as a function of AoA and drag polar for the model with Gurney flaps at $Re_c = 4.74 \times 10^5$. The C_L curve is shifted up depending on the Gurney flap height, but C_D increases considerably except for the cases with 1.2%c and 2.0%c. The drag coefficient is plotted as a function of the lift coefficient squared, as shown in Fig. 10(a). The plots for the heights 1.2%c and 2%c are close to that for the baseline model, while other curves are considerably

shifted and the slope is also changed. This indicates that the zero-lift drag coefficient increases and Oswald efficiency varies for Gurney flaps. These results are similar to the previously published data for a NACA0012 airfoil [7]. The lift-to-drag ratio is plotted in Fig. 10(b) as a function of C_L. Unlike SETE, the L/D curves are not collapsed, and they are lower than the baseline data. Figure 11 shows a direct comparison between a 10%c SETE with a 5^o deflection angle and a 1.2%c Gurney flap. The vertical displacement of the tip of the SETE is about 0.87%c that is close to the Gurney flap height 1.2%c. The lift enhancements in the both cases are almost the same, but the Gurney flap suffers from a larger drag penalty, giving a smaller L/D than that for the SETE for all positive C_L.

To evaluate the net benefit of flow control in terms of the power required for cruise flight, Liu [19] has proposed the following weight criterion

$$\left[1+\frac{6}{7}\left(\frac{\eta_{FC,r}}{b}\frac{C_L^{3/2}}{C_D}\right)W^{-1/6}\right]^{-1}\left(-\frac{6}{7}\frac{\Delta C_D}{C_D}+\frac{9}{7}\frac{\Delta C_L}{C_L}\right)-\frac{\Delta W}{W}>0\,, \tag{2}$$

where $\Delta W/W$ is the ratio between the control system weight ΔW and the total aircraft weight W, and $\eta_{FC,r}=P_{FC,r}/\Delta W$ is the actuating power density. For an ideal, weightless passive control device, the criterion is reduced to

$$-\frac{6}{7}\frac{\Delta C_D}{C_D}+\frac{9}{7}\frac{\Delta C_L}{C_L}=g>0\,. \tag{3}$$

The function g is interpreted as a benefit margin for flow control. When g is positive, less engine power is required for cruise flight with a passive flow control device like SETE and Gurney flap, and therefore the net benefit is achieved. Figure 12 shows the benefit margin for SETE and Gurney flaps. For the SETE of the 10%c length and deflection angle of 5^o, its benefit margin remains positive and approaches to zero as AoA reaches to 13^o. This further confirms the feasibility of this SETE for improving the cruise flight efficiency. In contrast, for the 10%c SETE with a deflection of 14^o, the benefit margin becomes negative at about 5^o of AoA. The Gurney flap with the 1.2%c height has a similar behavior, while for the Gurney flap with the 4.12%c height g is considerably below zero after about 3^o of AoA.

(a) (b)

Figure 8. (a) Schematic of a main airfoil with a Gurney flap, (b) NACA0012 airfoil model with a Gurney flap.

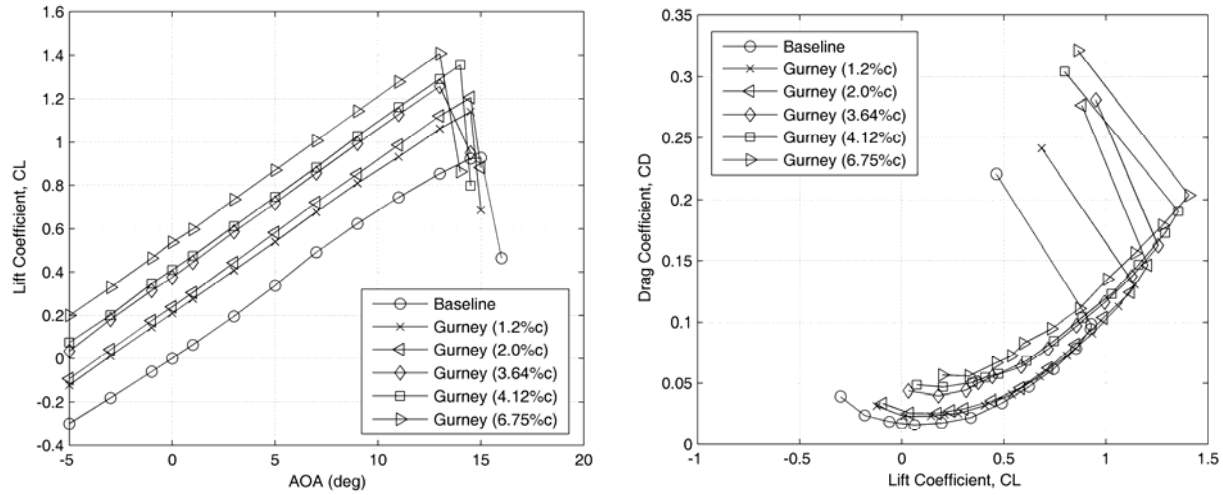

(a) (b)

Figure 9. (a) Lift coefficient and (b) drag coefficient as a function of AoA for the NACA0012 airfoil model with Gurney flaps at $Re_c = 4.74 \times 10^5$.

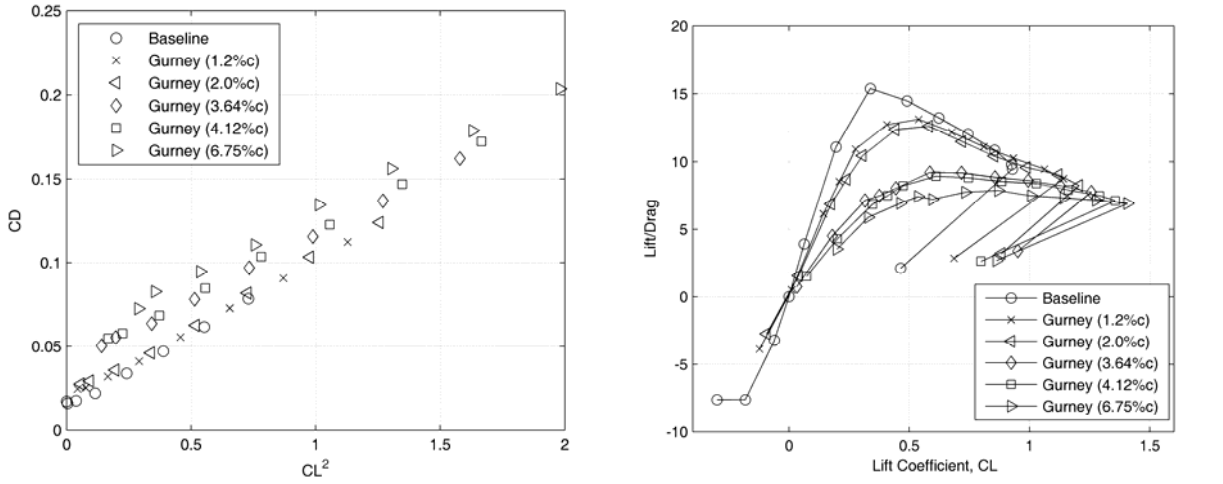

(a) (b)

Figure 10. (a) Drag coefficient as a function of the lift coefficient squared, (b) Lift-to-drag ratio as a function of the lift coefficient for the NACA0012 airfoil model with Gurney flaps at $Re_c = 4.74 \times 10^5$.

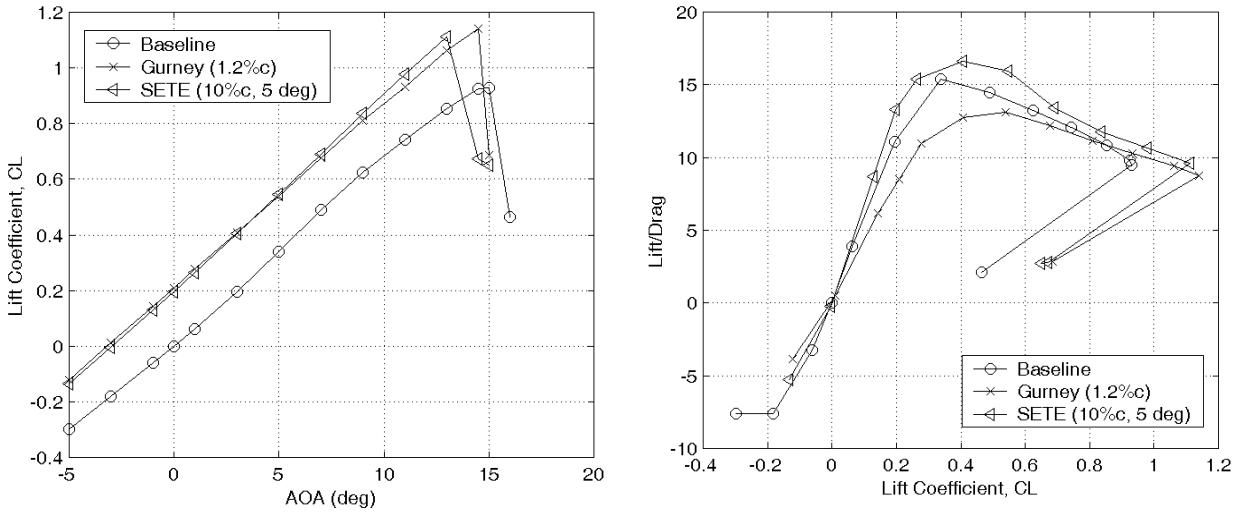

(a) (b)

Figure 11. Comparison between SETE and Gurney flap on (a) the lift coefficient as a function of AoA, and (b) the lift-to-drag ratio as a function of the lift coefficient squared for the NACA0012 airfoil model at $Re_c = 4.74 \times 10^5$ **.**

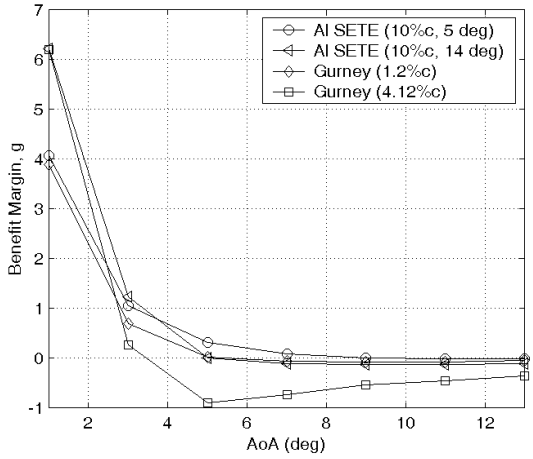

Figure 12. Benefit margins of SETE and Gurney flaps for cruise flight.

Thin Airfoil Theory

Like conventional flaps, the lift enhancement by SETE is generated by a change of the camber at the trailing edge. For geometrical simplicity, the main wing and SETE are modeled by straight segments, as shown in Fig. 1(b). The total projected chord is $c' = c + l\cos\delta$. The slopes of the chord line segments are 0 for $0 \le x < c$ and $-\tan\delta$ for $c \le x < c'$. According to the classical thin airfoil theory assuming that the slope is small [20], the strength of the vortex sheet is

$$\gamma(\theta) = 2U_\infty \left(A_0 \frac{1+\cos\theta}{\sin\theta} + \sum_{n=1}^{\infty} A_n \sin n\theta \right), \tag{4}$$

where the angular variable is related the main chordwise coordinate by $x = (c'/2)(1-\cos\theta)$. The coefficients in Eq. (4) are $A_0 = \alpha + \tan\delta(1-\theta_c/\pi)$ and $A_n = (2/\pi n)\tan\delta \sin(n\theta_c)$ $(n = 1,2,\cdots)$. Here the angular variable θ_c,

which corresponds to the breaking point between the main wing and SETE, is given by $\theta_c = cos^{-1}\left[(\varepsilon-1)/(\varepsilon+1)\right]$, where $\varepsilon = (l/c)cos\delta$.

The sectional lift coefficient is given by

$$C_l = \frac{L'}{(1/2)\rho_\infty U_\infty^2 c} = 2\pi(1+\varepsilon)\left[\alpha + tan\delta\left(1-\theta_c/\pi + sin\theta_c/\pi\right)\right]. \quad (5)$$

The positive deflection angle of SETE shifts the C_l curve upward (lift enhancement) and slightly increases the lift slope. The moment coefficient around the 1/4 total chord is

$$C_{m,c'/4} = \frac{M'_{c'/4}}{(1/2)\rho_\infty U_\infty^2 c^2} = (1/4)(1+\varepsilon)^2 tan\delta\left(sin2\theta_c - 2sin\theta_c\right), \quad (6)$$

where $C_{m,c'/4}$ is defined to be positive when it makes the leading edge up. Clearly, the positive deflection angle produces a negative moment. Furthermore, the pressure coefficient difference between the pressure and upper surfaces of the airfoil is $\Delta C_p = 2\gamma(x)/U_\infty$.

For a finite rectangular wing, the effective angle of attack is $\alpha - (1+\tau)C_L/\pi AR$, where AR is the effective aspect ratio and the parameter τ is a function of $AR/2\pi$ for a rectangular wing [21]. A convenient regression formula is $\tau = -0.0476(AR/2\pi)^2 + 0.2195(AR/2\pi)$ for $AR/2\pi \in [0.25, 1.75]$. Hence, the lift enhancement $\Delta C_L = C_L - C_{L,baseline}$ for a finite rectangular wing can be calculated, where the lift coefficient for the wing with SETE and baseline wing are, respectively,

$$C_L = \left[1 + \frac{2(1+\tau)}{AR}\right]^{-1} C_l, \quad (7)$$

and

$$C_{L,baseline} = \left[1 + \frac{2(1+\tau)}{AR}\right]^{-1} 2\pi\alpha. \quad (8)$$

According to the above relations, the lift enhancement by SETE is

$$\Delta C_L = 2\left[1 + \frac{2(1+\tau)}{AR}\right]^{-1}\left[\pi\varepsilon\alpha + (1+\varepsilon)tan\delta\left(\pi - \theta_c + sin\theta_c\right)\right]. \quad (9)$$

The difference of the pressure coefficient between the pressure and upper surfaces of the main wing is sensitively affected by SETE. These results indicate a direct correlation of the aerodynamic loading between the main airfoil and SETE. Figure 13 is a comparison between the predicted ΔC_L by thin airfoil theory and experimental and CFD data for the NACA0012 airfoil section ($AR = 4.42$, $l/c = 0.1$) with SETE. The near-linear relation given by thin airfoil theory reasonably describes the initial trend of the experimental results for small deflections. However, the experimental data saturate as the deflection angle increases further, which may be caused by a reduced effective deflection due to viscous effect. Two-dimensional CFD calculations using a Navier-Stokes code (Fluent), assuming that the boundary layer on the NACA0012 airfoil with SETE is fully turbulent, predict the smaller lift enhancement.

Thin airfoil theory has been expanded for the lift problem of an airfoil with a Gurney flap [22]. A solution of the generalized thin-airfoil integral equation for the vortex strength can be obtained by the method of successive approximations. The Gurney flap lift enhancement is interpreted as a special camber effect. The lift coefficient increment (pitching moment as well) is given as a square-root function of the relative Gurney flap height, i.e., $\Delta C_L \propto \sqrt{h/c}$. For comparison with Gurney flap, the vertical displacement of SETE is defined as $h/c = (l/c)sin\delta$. Therefore, ΔC_L by SETE depends on the relative length l/c and deflection angle δ. Figure 14 shows the normalized ΔC_L as a function of h/c for SETE and Gurney flap according to thin airfoil theory. Interestingly, ΔC_L increases in a linear fashion as an increase of the deflection angle for SETE with a fixed length,

while ΔC_L follows a square-root relation for both Gurney flap and SETE with a variable length for a fixed deflection angle.

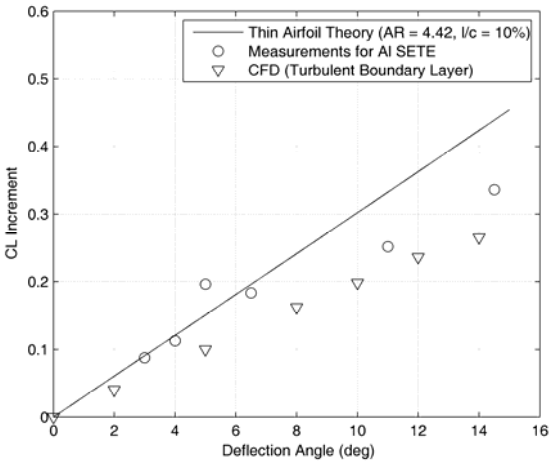

Figure 13. Measured lift enhancement compared with thin airfoil theory and CFD data for the NACA0012 airfoil model with SETE.

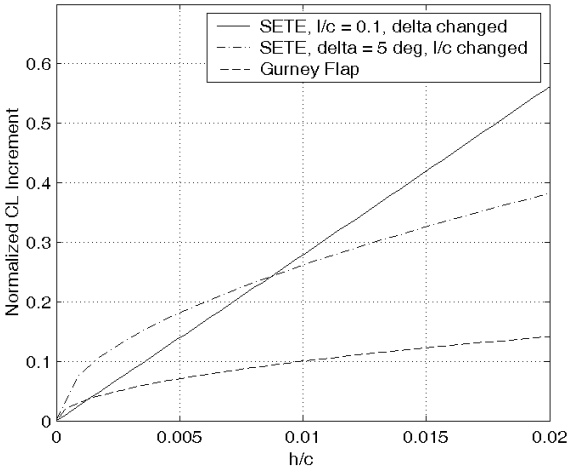

Figure 14. Comparison of normalized lift enhancement between SETE and Gurney flap based on thin airfoil theory.

Deformation and Bending Moment

The aluminum and Mylar sheets as SETE are usually set at nominal deflection angles in experiments assuming they are sufficiently rigid. Nevertheless, small aeroelastic deformation relative to the neutral position always exists. To estimate the elastic deformation of SETE, we consider a 2D clamped thin plate deformed due to aerodynamic load. The non-dimensional deformation $\overline{w} = w/l$ is given by

$$\overline{w}(\overline{x}) = G_1^{-1}\int_0^{\overline{x}} d\overline{x}_1 \int_0^{\overline{x}_1} d\overline{x}_2 \int_0^{\overline{x}_3} d\overline{x}_3 \int_0^{\overline{x}_3} \Delta C_p(\overline{x}_4)\, d\overline{x}_4 + A\overline{x}^3/6 + B\overline{x}^2/2\,, \tag{10}$$

where $\overline{x} = x/l$ is the normalized chordwise coordinate from the breaking point between the main element and SETE, $G_1 = D_E/(l^3 q_\infty)$, $A = 2G_1^{-1}(g_1 - g_2)$, $A = G_1^{-1}(g_2 - 2g_1)$, and

$$g_1 = \int_0^1 d\overline{x}_1 \int_0^{\overline{x}_1} d\overline{x}_2 \int_0^{\overline{x}_2} \Delta C_p(\overline{x}_3)\, d\overline{x}_3\,,$$

$$g_2 = \int_0^1 d\overline{x}_1 \int_0^{\overline{x}_1} \Delta C_p(\overline{x}_2)\, d\overline{x}_2\,.$$

The pressure coefficient difference $\Delta C_p = 2\gamma(x)/U_\infty$ from thin airfoil theory is substituted into Eq. (10) and numerical integration is carried out. Figure 15 shows the normalized deformation $\overline{w}/\sin\delta$ as a function of $\overline{x} = x/l$ for the 0.216 mm thick aluminum sheet ($G_1 = 5.74$, 10%c) and 0.254 mm thick Mylar sheet ($G_1 = 0.38$, 10%c). The deformation of the aluminum SETE is less than 1% of the vertical tip displacement $l\sin\delta$, while for the Mylar SETE it could be 13%. To estimate the actuating power required for deflecting SETE, the bending moment relative to the breaking point between the main element and SETE is estimated. The bending moment coefficient is defined as

$$C_{M_b} = \frac{M_b}{q_\infty l^2} = \int_0^1 \Delta C_p(\overline{x})\,\overline{x}\, d\overline{x}\,.$$

Figure 16 shows the bending moment coefficient as a function of AoA for SETE with a deflection angle of 5 degrees. The bending moment for the 2D case is in the order of $q_\infty l^2$.

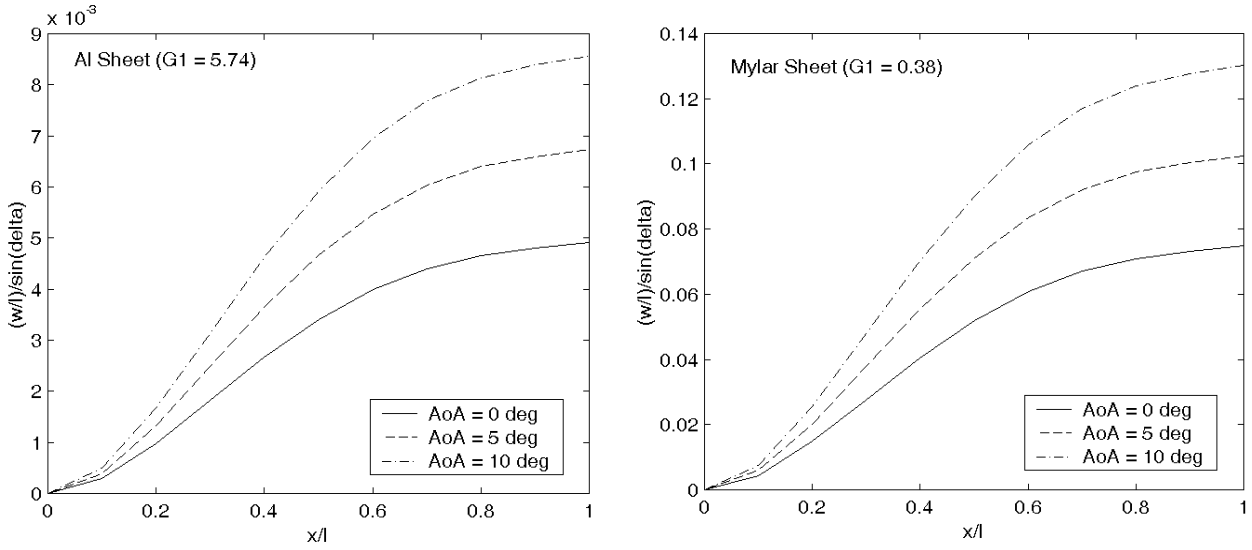

Figure 15. Normalized deformation of the aluminum SETE and Mylar SETE with a deflection angle of 5 degrees for different AoAs.

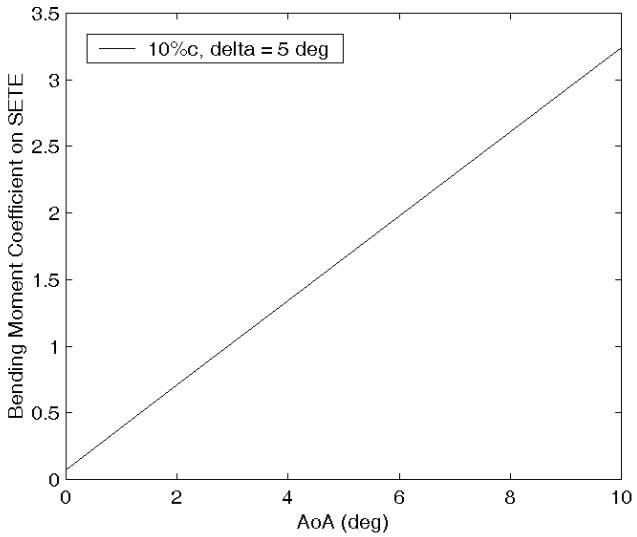

Figure 16. Bending moment of SETE with a deflection angle of 5 degrees relative the breaking point between the main element and SETE.

CFD Simulations

In order to provide further insights to the lift enhancement by SETE, the flow characteristics around a NACA0012 airfoil with SETE were studied using CFD simulations $Re_c = 4.74 \times 10^5$. The problem of a steady turbulent flow over the airfoil was solved using the commercial code Fluent on a C-grid. Grid independence was validated by comparing pressure distributions along the airfoil at two different angles of attack with published results [23]. The

lift and drag coefficients were also compared with the published data [23]. The boundary layers were assumed to be fully turbulent, and the realizable k-epsilon turbulence model with the non-equilibrium wall function was used.

Figure 17 shows how the defection angle of SETE affects the pressure coefficient distribution on the airfoil for zero AoA. The aerodynamic loading on SETE itself ($x/c>1$) is not large, and the lift enhancement is mainly produced by the overall aerodynamic change on the main airfoil induced by SETE. Comparisons of the calculated and measured lift coefficients are shown in Fig. 18 as a function of AoA. The calculated results for the 2D airfoil are converted to the 3D wing results using Eq. (7). The calculated and experimental results are consistent until the calculated lift coefficients level at higher AoAs. As indicated in Fig. 13, the calculated increment in the lift coefficient exhibits the same trend as the experimental and theoretical results as a function of the deflection angle of SETE. Figure 19 shows velocity magnitude contours around the NACA0012 airfoil with zero AoA for 0^o and 5^o deflection angles. The asymmetry of the flow field is induced by SETE and the wake is turned downward, indicating a deflected momentum stream tube and the generation of additional lift. The wake structure is not appreciably altered although it is deflected; this implies that the parasite drag is not significantly affected.

Further, a 10%c SETE with a 5^o deflection angle is compared with a conventional plain flap that is deflected at the 90% chord of a NACA0012 airfoil. Figure 20 shows the computed lift and drag coefficients as a function of the deflection angle for the SETE and corresponding plain flap. Compared with the plain flap, the lift enhancement by the SETE is larger while the drag coefficient is smaller. Here the lift and drag coefficient for the SETE is defined based on the main airfoil chord *c*. Even when these coefficients are based on 1.1c for the SETE, the above results are still qualitatively valid. The pressure coefficient distributions on the main airfoil for the SETE (5^o deflection), plain flap (5^o deflection) and Gurney flap are shown in Fig. 21, indicating that the larger pressure difference on the main airfoil is induced by the SETE. The Gurney flap height is $0.1c\sin(5^o)\approx 0.87\%c$, which is the same as the maximum vertical displacement of the SETE. Figures 22 and 23 show the lift coefficient as a function of AoA and the drag polar for the SETE, plain flap and Gurney flap. Among these trailing edge devices, the SETE generates the largest lift increase at a smallest drag penalty. It should be emphasized here that the absolute accuracy of the drag predicted by CFD is not critically examined although the computed drag coefficient for the NACA0012 airfoil is close to $C_D = 0.02 - 0.03$ given by measurements for the corresponding airfoil section. Therefore, the above comparison in the drag polar is valid only in a relative sense. Furthermore, for the 2D airfoil, the drag polar is not parabolic since no induced drag is included.

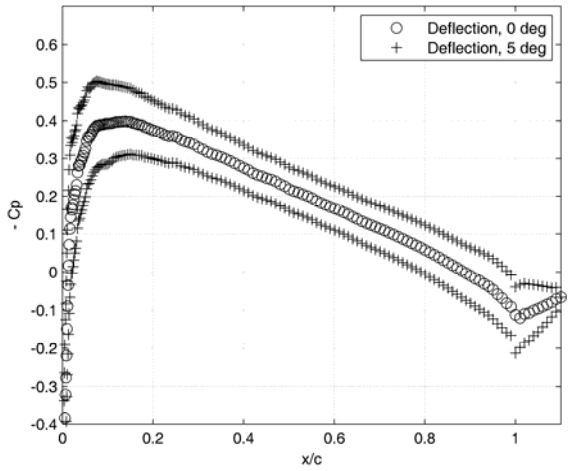

Figure 17. Calculated pressure coefficient distributions on the NACA0012 airfoil for the SETE deflection angles of 0 and 5 degrees at zero AoA.

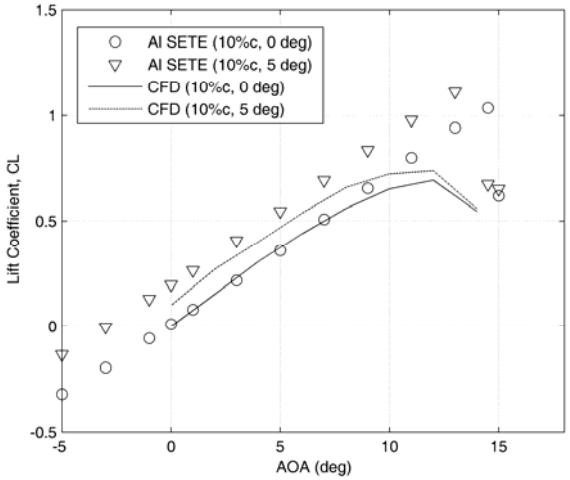

Figure 18. Comparisons of the calculated and measured lift coefficients as a function of AoA for the deflection angles of 0 and 5 degrees.

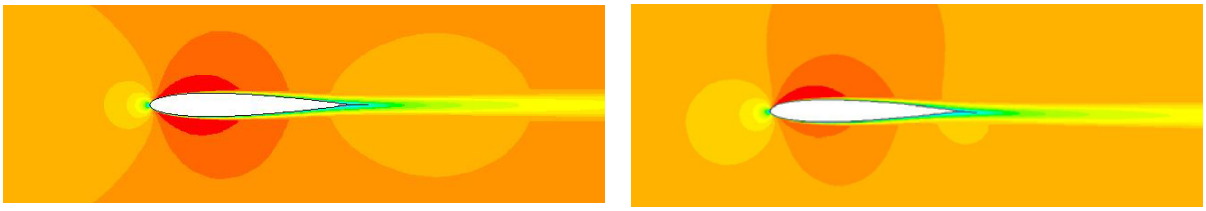

(a) (b)

Figure 19. Velocity magnitude fields of the NACA0012 airfoil at zero AoA, (a) zero deflection of SETE, (b) 5 degrees deflection of SETE.

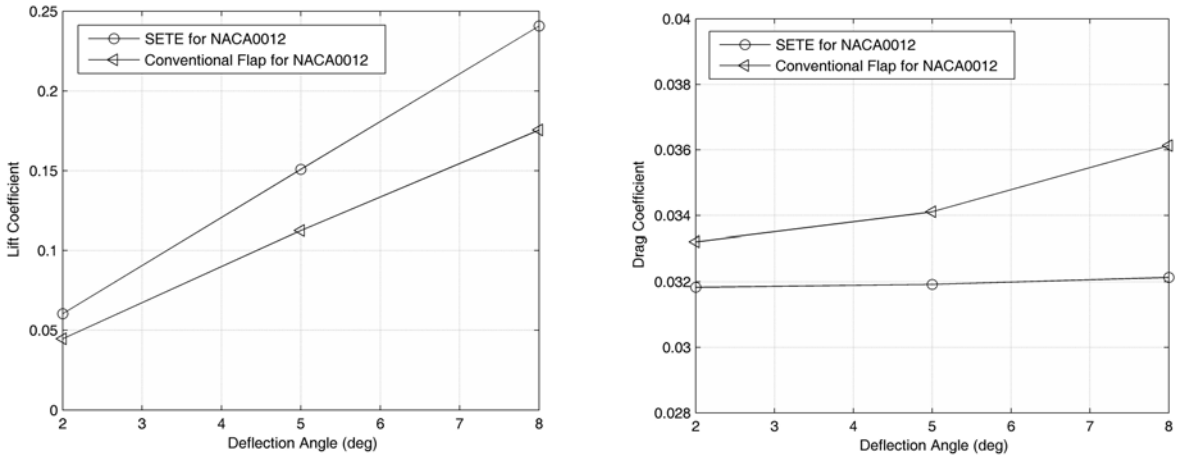

(a) (b)

Figure 20. Comparison of the computed lift and drag coefficients between SETE and conventional flap for a NACA0012 airfoil at zero AoA.

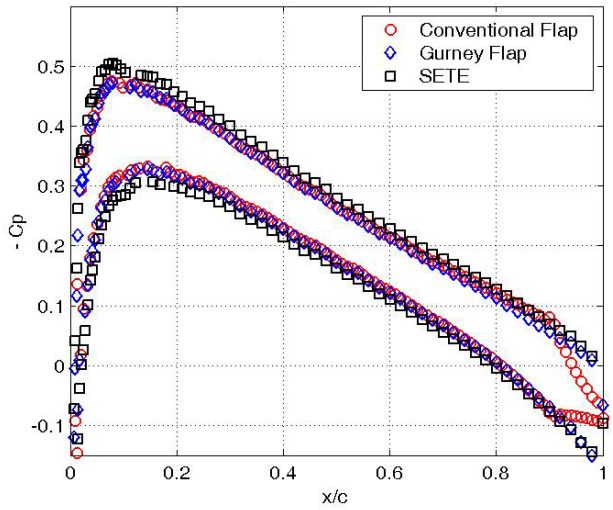

Figure 21. Comparison of the computed pressure coefficient between SETE, conventional flap and Gurney flap for a NACA0012 airfoil at zero AoA.

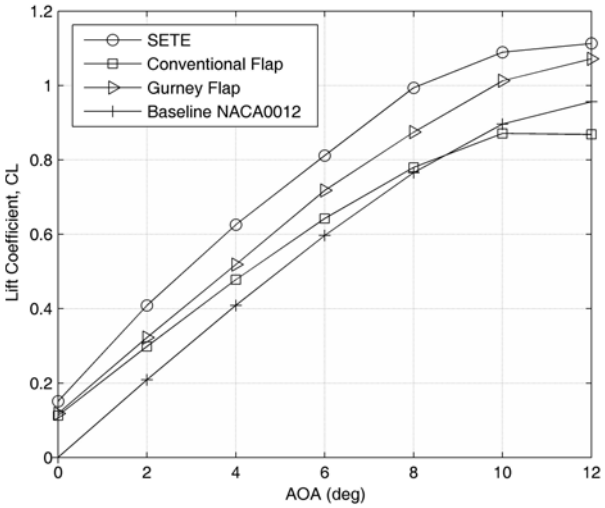

Figure 22. The computed lift coefficient as a function AoA for SETE (5-deg deflection), Gurney flap and conventional flap (5-deg deflection) for a NACA0012 airfoil.

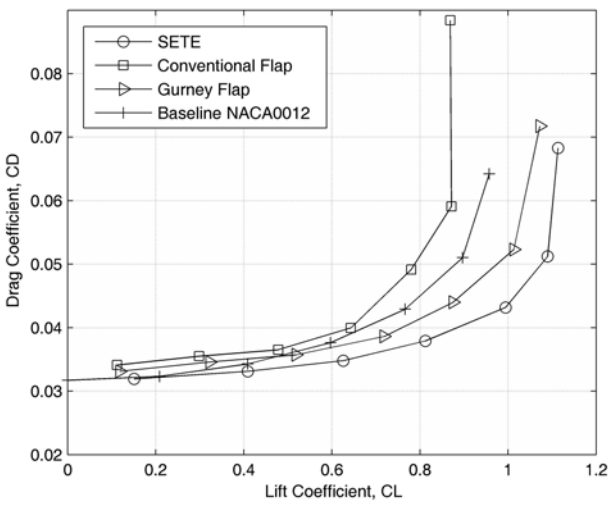

Figure 23. The computed drag polar for SETE (5-deg deflection), Gurney flap and conventional flap (5-deg deflection) for a NACA0012 airfoil.

Conclusions

Experiments and calculations presented show that a static extended trailing edge (SETE) attached to a NACA0012 airfoil model is able to enhance the lift while the zero-lift drag is not significantly increased. The mechanism of lift enhancement by SETE is the camber effect, which is the same as that for other high-lift devices like Gurney flap and conventional flap. However, compared with Gurney flap and conventional flap, SETE generates a larger lift increase at a smaller drag penalty since it is embedded in the wake of the main airfoil. Therefore, SETE has a promising potential for improving the efficiency of cruise flight. The benefit margin of SETE for cruise flight is evaluated in comparison with Gurney flap, and the feasibility of SETE for lift enhancement in cruise flight is demonstrated at small angles of attack and deflection angels of SETE. The mechanical simplicity of SETE allows direct application to aircraft without changing the basic aerodynamic configuration. Furthermore, the deformation and pitching moment of SETE due to aerodynamic loading are estimated, and actuating SETE is feasible since the pitching moment on it is small. Future research will focus on SETE actuation using smart material like piezoactuators and shape memory alloys for steady and unsteady flow control.

References

[1] Liebeck, R. H., "Design of Subsonic Airfoils for High Lift," Journal of Aircraft, Vol. 15, No. 9, 1978, pp. 547-561.

[2] Storms, B. and Jang, C. S., "Lift Enhancement of an Airfoil Using a Gurney Flap and Vortex Generators," Journal of Aircraft, Vol. 31, No. 3, 1994, pp. 542-547.

[3] Ross, J., Storms, B. L. and Carrannanto, P. G., "Lift-Enhancing Tabs on Multielement Airfoils," Journal of Aircraft, Vol. 32, No. 3, 1995, pp. 649-655.

[4] Myose, R., Papadakis, M. and Heron, I., "Gurney Flap Experiments on Airfoils, Wings, and Reflection Plane Model," Journal of Aircraft, Vol. 35, No. 2, 1998, pp. 206-211

[5] Jang, C. S., Ross, J. C. and Cummings, R. M., "Numerical Investigation of an Airfoil with a Gurney Flap," Aircraft Design, Vol. 1, 1998, pp. 75-88.

[6] Jeffrey, D., Zhang, X. and Hurst, D. W., "Aerodynamics of Gurney Flaps on a Single-Element High-Lift Wing," Journal of Aircraft, Vol. 37, No. 2, 2000, pp. 295-301.

[7] Li, Y., Wang, J. and Zhang, P., "Effects of Gurney Flaps on a NACA0012 Airfoil," Flow, Turbulence and Combustion, Vol. 68, No.1, 2002, pp. 27-39.
[8] Gai, S. L. and Palfrey, R., "Influence of Trailing-Edge Flow Control on Airfoil Performance," Journal of Aircraft, Vol. 40, No. 2, 2003, pp. 332-337
[9] Meyer, R., Hage, W., Bechert, D. W., Schatz, M. and Thiele, F., "Drag Reduction on Gurney Flaps by Three-Dimensional Modification," Journal of Aircraft, Vol. 43, No. 1, 2006, pp. 132-140.
[10] Bechert, D. W., Stanewsky, E. and Hage, W., "Wind Tunnel Measurements on a Transonic Wing with Flow Control by Various Devices," DLR Internal Report DLR-IB 223-99C05/IB 92517-99/b3-2, June 1999.
[11] Storms, B. and Ross, J., "Experimental Study of Lift-Enhancement Tabs on a Two-Element Airfoil," Journal of Aircraft, Vol. 32, 1995, pp. 1072-1078.
[12] Lee, H. T., Kroo, I. M., and Bieniawski, S., "Flutter Suppression for High Aspect Ratio Flexible Wings Using Microflaps," AIAA Paper 2002-1717, Denver, CO; 22-25 Apr. 2002.
[13] Bechert, D. W., Bruse, M., Hage, W., and Meyer, R., "Biological Surfaces and their Technological Applications — Laboratory and Flight Experiments on Drag Reduction and Seperation Control," AIAA Paper 97-1960, 1997.
[14] Stanewsky, E., "Adaptive Wing and Flow Control Technology," Progress in Aerospace 37, 2001, pp. 583-667
[15] Liu, T., Kuykendoll, K., Rhew, R. and Jones, S., "Avian Wing Geometry and Kinematics," AIAA Journal, Vol. 44, No. 5, 2006, pp. 954-963.
[16] Liu, T., Montefort, J., Woodiga, S., Merati, P. and Shen, L., "Global Luminescent Oil Film Skin Friction Meter," AIAA Journal (in preparation) 2007.
[17] Meirovitch, L. "Analytical Methods in Vibrations," The Macmillan Company, New York, 1967.
[18] McCormick, B. W., "Aerodynamics, Aeronautics, and Flight Mechanics (Second Edition)," John Wiley & Sons, New York, 1995, p. 116.
[19] Liu, T., "Weight Criterion on Flow Control in Flight," Journal of Aircraft, Vol. 44, No. 1, 2007, pp. 348-351
[20] Anderson, J. D., "Fundamentals of Aerodynamics (Second Edition)," McGraw-Hill, New York, 1984, Chapter 4.
[21] Glauert, H., The Element of Aerofoil and Airscrew Theory (Second Edition), Cambridge University Press, Cambridge, 1999.
[22] Liu, T. and Montefort, J., "Thin-Airfoil-Theoretical Interpretation for Gurney Flap Lift Enhancement," Journal of Aircraft, Vol. 44, No. 2, pp. 667-671, 2007.
[23] Hegna, H. A., "A Numerical Solution of Incompressible Turbulent flow over Airfoils", AIAA Paper 1981-47, St. Louis, MO, Jan. 12-15, 1981.